ADVANCED ENERGY MATERIALS
www.advenergymat.de

Flocculating-Regulated TiO_2 Deposition Enables the Synergistic Effect of Doping for Perovskite Solar Cells with Efficiency Exceeding 25.8%

*Huilin Yan, Xing Zhao, Hao Huang, Danxia Wu, Pengkun Zhu, Danni Li, Bingbing Fan, Yujie Qiu, Yuqing Yang, Qi Geng, Peng Cui, Yingying Yang, Zhineng Lan, and Meicheng Li**

The planar perovskite solar cells (PSCs) using TiO_2 as the electron transport layer (ETL) are undergoing a stagnated efficiency improvement, which the inferior TiO_2 ETL mainly limits. Herein, a flocculating-regulated TiO_2 deposition using $SnCl_2{\cdot}2H_2O$ is reported as the flocculate to control the nanoparticle size finely for optimizing TiO_2 deposition and to achieve a synergistic Sn doping. The $SnCl_2{\cdot}2H_2O$ incorporated into bath precursor can bridge-link the suspended nanoparticles, which promotes the precipitation of large-sized nanoparticles and leaves the smaller-sized nanoparticles for deposition, leading to a compact TiO_2 film with marked reduced surface roughness. Meanwhile, along with flocculating-regulated TiO_2 deposition, it can also be achieved the Sn-doping of TiO_2, which increases the conductivity of TiO_2 thin films by ≈2.5 times. As a consequence, attributing to the optimized interface contact and accelerated interfacial electron transport, the planar PSCs achieved a certification efficiency of 25.85%, the highest value among the TiO_2-based planar PSCs to date. In addition, the PSCs can maintain 99% of their initial efficiency after more than 4500 h of storage in ambient air, showing excellent stability.

1. Introduction

Perovskite solar cells (PSCs), as an emerging photovoltaic technology, have developed rapidly with the latest certificated power conversion efficiency (PCE) of 26.15%.[1] In n-i-p planar PSCs, the electron transport layer (ETL) plays a crucial role in realizing high PCE since it is responsible for extracting and transporting photo-generated electrons. Among various ETLs, SnO_2, TiO_2, and ZnO are the most commonly used electron transport materials.[2–4] At present, SnO_2-based planar PSCs have achieved a PCE of more than 26%.[5] However, as for the TiO_2, a more inexpensive and reserved-abundant material, the corresponding planar PSCs only obtain a PCE of 25.76% with a lower certificated PCE of 25.38%.[6] This inferior photovoltaic performance should result from the property of TiO_2 film and its interfacial contact property. The TiO_2-based PSCs are reported to suffer from strong electron accumulation and low open-circuit voltage due to the low conductivity of TiO_2 ETL, and its mismatched band alignment with the perovskite.[7,8]

To enhance the quality of TiO_2 ETL, researchers have extensively explored various deposition techniques, including spin-coating, spray pyrolysis, and chemical bath deposition (CBD).[9–11] Notably, CBD possesses the advantages of low-temperature and conformal deposition, making it particularly suitable for light-managing textured substrates like fluorine-doped tin oxide (FTO). However, this method still faces challenges with low-temperature processes, such as unmanageable crystal nucleation and orientation,[12] as well as a strongly corrosive acidic environment (pH < 0.5), which can decompose many organic or inorganic additives. Several strategies have been applied to regulate the TiO_2 deposition during the CBD method. Huang et al. introduced a ligand engineering strategy to finely tune the TiO_2 film and interface structures, achieving a peak power conversion efficiency (PCE) of 24.8%.[13] Wu et al. proposed a mild continuous pH control strategy for effectively regulating the hydrolysis process of $TiCl_4$ post-treatment, achieving the efficiency of the carbon electrode-based PSC of 18.08%.[14] Although TiO_2-based PSCs fabricated using the CBD method have achieved the highest reported efficiency of 25.76%,[6] there is still a gap in efficiency compared to SnO_2-based PSCs. Consequently, based on the strategy to regulate the TiO_2 deposition, further improving the electrical performance of TiO_2 is still necessary for enhancing the photovoltaic performance of TiO_2-based PSCs. Various attempts have been reported to modify TiO_2 properties in past years.[15–18] Among these attempts, doping has been substantiated as an efficacious approach for regulating the energy levels and conductivity of TiO_2, including doping with metals (such as Mg, Zn, Ag, Li, Rb, Ta, Nb, etc.[19–24]) and nonmetals (such as F, Cl, N, etc.[25–27]). However, few studies have mentioned and achieved a balance between the deposition and

H. Yan, X. Zhao, H. Huang, D. Wu, P. Zhu, D. Li, B. Fan, Y. Qiu, Y. Yang, Q. Geng, P. Cui, Y. Yang, Z. Lan, M. Li
State Key Laboratory of Alternate Electrical Power System with Renewable Energy Sources
North China Electric Power University
Beijing 102206, China
E-mail: mcli@ncepu.edu.cn

The ORCID identification number(s) for the author(s) of this article can be found under https://doi.org/10.1002/aenm.202403200

DOI: 10.1002/aenm.202403200

doping processes of TiO_2 in low-temperature chemical bath preparation to achieve synergistic optimization. Building upon the insights above, we believe that the synergistic integration of deposition control and doping could represent an effective strategy for acquiring high-quality TiO_2 ETL, thereby enhancing the performance of PSCs for various applications.

Herein, we synchronously realize the deposition regulation and doping of TiO_2 by incorporating $SnCl_2{\cdot}2H_2O$ aqueous solution to the chemical-bath precursor. The $SnCl_2{\cdot}2H_2O$ can agglomerate and remove the over-large size TiO_2 nanoparticles through a flocculating effect, leaving the suitable-sized TiO_2 nanoparticles for deposition. This flocculating-effect regulated deposition can deposit smaller nanoparticles and achieve a compact TiO_2 film with reduced surface roughness. Meanwhile, the $SnCl_2$ can also participate in hydrolysis, in which Sn^{2+} ions can successfully incorporate into the TiO_2 lattice, thereby increasing its conductivity for better charge carrier transport. Based on this modified Sn-doped TiO_2 ETL, the planar PSC achieves a certificated PCE of 25.85%, which is the highest value reported for TiO_2-based planar PSCs so far. In addition, the planar PSCs also exhibit enhanced stability with negligible efficiency decline after storage in ambient air over 4500 h.

2. Results and Discussion

2.1. Deposition and Characterization of TiO_2 ETLs

Here, we deposited TiO_2-based ETLs using a feasible CBD method using $TiCl_4$ as a Ti source.[7] Referring to the SnO_2 deposition using the $SnCl_2{\cdot}2H_2O$ as the precursor, where the hydrolysis of $SnCl_2$ is similar to the $TiCl_4$, but requires a higher temperature and longer time.[28] We attempt to incorporate $SnCl_2{\cdot}2H_2O$ into TiO_2 chemical-bath precursor, longing to regulate TiO_2 deposition and its electrical properties synchronously. The optimal concentration of $SnCl_2{\cdot}2H_2O$ was determined to be 0.5 mol% of $TiCl_4$ for achieving high-performance ETL, and the details are shown in the experimental section and Figure S1 (Supporting Information). Specifically, the TiO_2 obtained through $SnCl_2{\cdot}2H_2O$ flocculating regulation is hereafter named as FR-TiO_2.

To systematically explore the influence of $SnCl_2{\cdot}2H_2O$ on TiO_2 film topography, we carried out the scanning electron microscope (SEM) to observe the morphology changes of TiO_2 and FR-TiO_2 films with different bath times. As shown in **Figure 1**a,b, we can observe the conformal growth of TiO_2 on the FTO substrate as the bath time increases to 5 min, and the incorporated $SnCl_2{\cdot}2H_2O$ mitigates the growth of TiO_2 nanoparticles. After 15 min of bath, both the TiO_2 and FR-TiO_2 nanoparticles begin to land on the surface of FTO, as shown in Figure 1c,d. At this stage, we observe that the size of FR-TiO_2 nanoparticles is smaller than that of TiO_2 nanoparticles. In Figure 1e,f, as the bath time increases to 25 min, we can observe the growth of deposited TiO_2 and FR-TiO_2 nanoparticles, and the continuous film begins to form on the substrate. However, it is worth noting that the TiO_2 nanoparticles begin to agglomerate at this stage, which is supposed to further impact TiO_2 film topography in the following deposition process. When the bath time is 35 min (Figure 1g,h), the TiO_2 film possesses a rough surface with needle-like aggregates. In comparison, the FR-TiO_2 film is smoother with reduced particle aggregation. In the FR-TiO_2 film, we can still capture the outline of FTO grains, which is completely hidden under the TiO_2 film, suggesting that the FR-TiO_2 film is more uniform and denser with a smaller thickness. This allows the FR-TiO_2 film to tightly adhere to both the FTO substrate and the perovskite film in the PSCs. Figure 1i,j show the cross-sectional SEM images of FTO/TiO_2 and FTO/FR-TiO_2, respectively, where the FR-TiO_2 film is thinner and denser with reduced surface nanoparticle aggregation, compared to the TiO_2 film, which is consistent with the surface SEM images shown in Figure 1a–h. The atomic force microscope (AFM) was also carried out to characterize the TiO_2 and FR-TiO_2 films. As shown in Figure 1k,l, FR-TiO_2 film exhibits smaller nanoparticle size with reduced aggregation, compared to TiO_2 film. In addition, the root mean square (RMS) was calculated to evaluate the surface roughness quantitatively. The surface RMS of the FR-TiO_2 films was 33.45 nm, which is much smaller than that (62.23 nm) of the TiO_2 film. Based on the above results, we can find that incorporating $SnCl_2{\cdot}2H_2O$ into the chemical bath precursor of TiO_2 can mitigate the TiO_2 growth, which decreases the size of the nanoparticle and reduces the surface aggregating, leading to a denser FR-TiO_2 film with a smoother surface.

The smaller grain size and fewer needle-like aggregates in FR-TiO_2 film demonstrated by SEM and AFM measurements seem to contradict the macro-scale phenomena observed during the bath processes. As shown in Figure S3 (Supporting Information), when incorporating the $SnCl_2{\cdot}2H_2O$ into the chemical bath precursor, the solution includes more suspended particles and its color turns from milky white to light yellow. After static settlement for 10 h, the sediment in the chemical bath precursor with $SnCl_2{\cdot}2H_2O$ is more than twice that in the control chemical bath precursor, making the precursor clearer. Dynamic light scattering (DLS) analysis was performed on the supernatant of the chemical bath precursor to quantitatively characterize the nanoparticle size. As shown in Figure 1m, after incorporating $SnCl_2{\cdot}2H_2O$, the nanoparticle size in the supernatant decreases significantly from 488–537 to 37–76 nm. These smaller nanoparticles are beneficial for depositing compact FR-TiO_2 film with a smooth surface. During the CBD process, the $TiCl_4$ will hydrolysis intensively as Equations S1–S3 (Supporting Information) and form suspended particles in the chemical bath precursor.[14] When placed on a substrate, the small-sized nanoparticles will preferentially deposit on the substrate through nucleation growth, driven by a decrease in free energy.[13] And large-sized ions tend to suspend in the solution, while large-sized aggregated particles will land on the substrate surface, driven by gravity, and this process occurs relatively late. After incorporating $SnCl_2{\cdot}2H_2O$, the Sn^{2+} ions can coordinate with the hydroxyl compounds[29] of $[Ti(OH)_nCl_m]^{2-}$, forming polar bridging structures, thereby promoting the large-sized aggregated particles. The schematic diagram of the $SnCl_2{\cdot}2H_2O$ regulated CBD process is shown in **Figure 2**, the addition of $SnCl_2{\cdot}2H_2O$ is just like a flocculant during hydrolysis, which can adsorb and bridge-link suspended TiO_2 particles, promoting the flocculation and precipitation of TiO_2 nanoparticles. After the CBD process, we obtain FR-TiO_2 film with larger coverage and denser grain density compared to TiO_2 film, as shown in Figures S4a,b and S5 (Supporting Information). When rinsing the different films under deionized water, the sediments attached to the substrate will be washed away and the FR-TiO_2 sample turns more transparent than the TiO_2 sample, which was well confirmed by SEM images in Figure 2 and

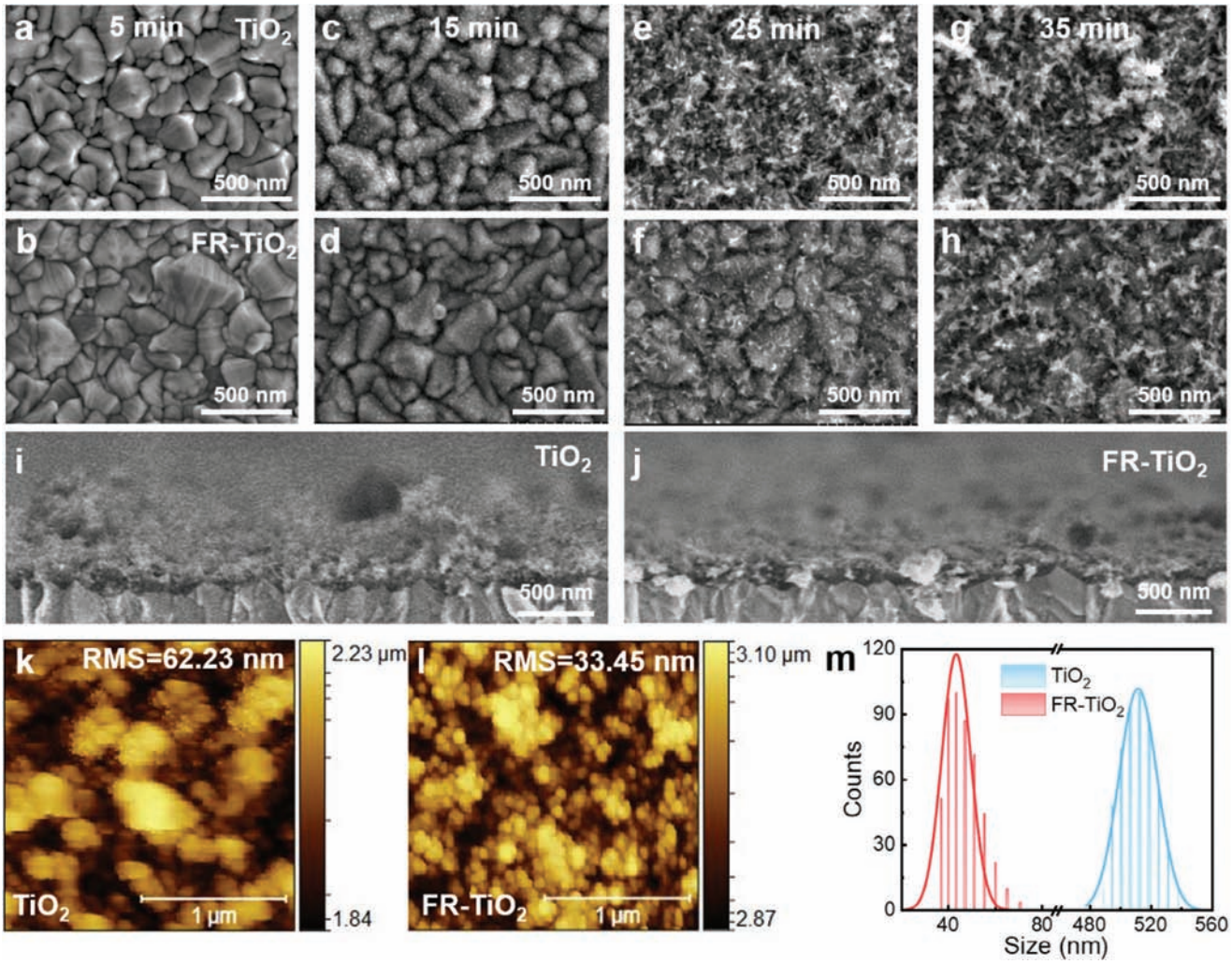

Figure 1. Topography characterization of TiO_2 and FR-TiO_2 films. a–h) Top-view SEM images of TiO_2 and FR-TiO_2 films in different bath times deposited on FTO. i,j) Cross-sectional SEM images of TiO_2 film and FR-TiO_2 film on FTO. k,l) AFM images of TiO_2 film, and FR-TiO_2 film, the graph size is 2×2 μm. m) DLS spectra of TiO_2 solution in CBD process with and without Sn source.

Figure S4c (Supporting Information). This flocculant effect can sift out the large particles and leave out the small nanoparticles to deposit, which is highly beneficial for the fabrication of smooth and compact FR-TiO_2 ETLs. Consequently, this method achieves smaller nanoparticle size with reduced aggregation, fewer pinholes, and tighter arrangement of the FR-TiO_2 film, which can effectively reduce leakage issues caused by direct contact between perovskite and the FTO substrate.

Now we turn to explore the Sn element doping and its influence on the electrical property of TiO_2. To confirm the presence of Sn in TiO_2, we first conducted energy dispersive X-ray spectroscopy (EDS) analysis on TiO_2 and FR-TiO_2 powders obtained by centrifuging the corresponding chemical bath precursor. From **Figure** 3a, we observe the existence of Sn element in the FR-TiO_2 powder, with the atom ratio of Sn increasing from 0 to 0.59%, as shown in Tables S1,S2 (Supporting Information). The X-ray photoelectron spectroscopy spectra performed directly on TiO_2 and FR-TiO_2 films also validate the existence of Sn in TiO_2. As shown in Figure 3b, the presence of Sn $3d_{5/2}$ and Sn $3d_{3/2}$ peaks at 485.55 and 493.95 eV, respectively, indicate the Sn dopant in TiO_2, consistent with the EDS results. In the Ti 2p spectrum shown in Figure 3c, after incorporating $SnCl_2{\cdot}2H_2O$ into bath precursor, the Ti $2p_{3/2}$ and Ti $2p_{1/2}$ peaks shift from 457.05 and 462.75 eV to the higher binding energy of 457.65 and 463.35 eV, respectively (Figure 3c). This shift is attributed to the higher electronegativity of Sn (1.96) compared to that (1.54) of Ti, indicating that Sn incorporates into the TiO_2 lattice, which can also be validated by the results of X-ray diffraction (XRD) measurements (Figure 3d).

A good ETL should meet conditions such as weak light absorption in the visible spectrum and high electrical conductivity. To explore the bandgap and light absorption of TiO_2 and FR-TiO_2, UV–vis absorption characterization was performed on Glass/FTO/TiO_2 and Glass/FTO/FR-TiO_2 (Figure S6a, Supporting Information). There is a blue shift in the absorption edge of FR-TiO_2 compared to TiO_2, with the bandgap increasing from 3.43 to 3.52 eV, which may be due to the quantum confinement effect of the smaller size of FR-TiO_2 particles.[30] A wider bandgap

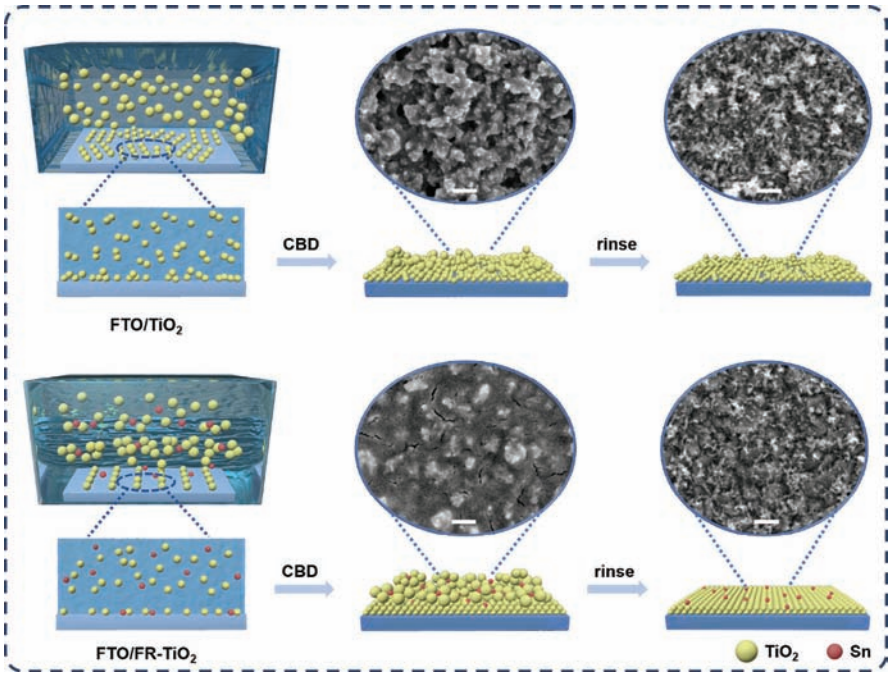

Figure 2. The schematic diagram with and without the $SnCl_2{\cdot}2H_2O$ regulated CBD process. All scale bars are 250 nm.

allows more light to penetrate the absorption layer, thereby enhancing the PSCs' efficiency in utilizing light. Then the UV photoelectron spectroscopy (UPS) measurements for TiO_2, FR-TiO_2, and perovskite films are shown in Figure 3f and Figure S6b (Supporting Information). The secondary electron cut-off ($E_{cut\text{-}off}$) edge of FR-TiO_2 shifts from 16.33 to 16.71 eV. We further calculate the valence band maximum energy (E_{VBM}) value of FR-TiO_2 to be 8.4 eV, and the E_{VBM} of TiO_2 to be 8.6 eV. Combining the results of UV–vis absorption characterization (Figure S6a, Supporting Information), we also calculate the conduction band minimum energy (E_{CBM}) value of TiO_2 to be 5.17 eV, and the E_{CBM} of FR-TiO_2 to be 4.88 eV. Based on the energy level information of ETLs and perovskite (Figure S6b, Supporting Information), the Energy level diagram of TiO_2, FR-TiO_2, and perovskite is depicted in Figure 3g. The energy level offset (ΔE = ECB Perovskite − ECB TiO2) is reduced from 0.44 to 0.15 eV, which suggests that the FR-TiO_2 is beneficial for interfacial electron transport. To characterize whether Sn doping can improve the conductivity of the TiO_2 ETL, the dark current densities of Glass/FTO/TiO_2/Au and Glass/FTO/FR-TiO_2/Au were measured (Figure 3e). Compared to the TiO_2 film, the conductivity of FR-TiO_2 increased ≈2.5 times higher than TiO_2. This indicates that Sn doping contributes to enhanced conductivity, possibly because Sn incorporates into the TiO_2 lattice. The higher conductivity of ETL helps to improve the electron transport within TiO_2, which is beneficial for accelerating electron transport and reducing hysteresis effects.

2.2. Optimized Optoelectronic Performance of Perovskite Film

We fabricated perovskite films on TiO_2 and FR-TiO_2 ETL substrates using a two-step spin-coating method,[31] followed by SEM, XRD, and UV–vis absorption analysis to observe the film properties. **Figure** 4a,b show SEM images of the perovskite films. Compared to TiO_2-based samples, the perovskite film deposited on FR-TiO_2 has larger grain sizes and fewer, smaller PbI_2 crystals[32] on its surface. XRD analysis in Figure 4e and Figure S7a (Supporting Information) indicates the perovskite film grown on FR-TiO_2 shows a significant decrease in the proportion of the PbI_2 peak at 12.8 degrees (Figure S7a, Supporting Information). Although residual PbI_2 is reported to passivate the perovskite defects, its instability, especially under illumination, will deteriorate the perovskite stability.[33,34] Hence, decreasing the amount of residual PbI_2 may contribute to an enhanced stability of perovskite film. Compared to the perovskite film on TiO_2, the perovskite film on FR-TiO_2 exhibits a higher proportion of the (111) plane at 24.5 degrees and a smaller full width at half maximum the of (111) plane (Figure S7b, Supporting Information), indicating an enhanced facet orientation and crystallinity. Figure 4c,d depict cross-sectional views of PSCs structured as FTO/ETLs/perovskite/2,2′,7,7′-tetrakis[N,N-di(4-methoxyphenyl)amino]-9-9′-spirobifluorene (Spiro-OMeTAD)/Au. The cross-sectional images show that the FR-TiO_2 film is thinner than the TiO_2 film, and the perovskite film exhibits tight and continuous contact with FR-TiO_2, which may result from the decreased surface roughness and a reduced contact angle, based on flocculating-regulated deposition (Figure S8, Supporting Information). UV–vis absorption characterization (Figure 4f) was also performed on perovskite films deposited on different ETLs. The absorption edge of perovskite film shows negligible change, but the absorption intensity of the perovskite film on FR-TiO_2 increases, indicating a higher quality of perovskite film.

To evaluate the defects density of perovskite films based on TiO_2 and FR-TiO_2, we prepared electron-only device structures as FTO/TiO_2 or FR-TiO_2/perovskite/[6,6]-phenyl-C61-butyric acid

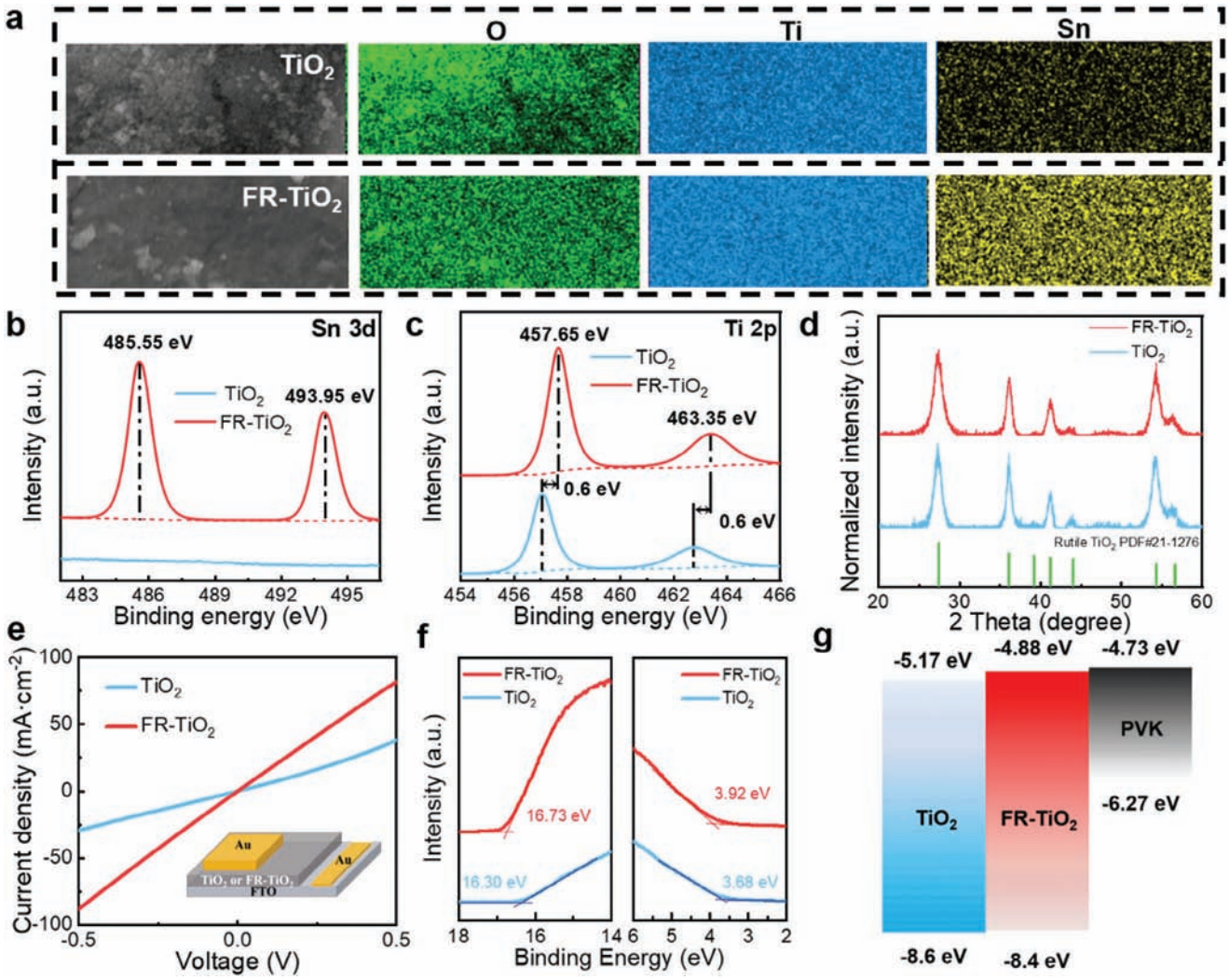

Figure 3. a) TiO2 and FR-TiO_2 powder and Elemental face mapping images. b,c) Sn 3d and Ti 2p spectra of TiO_2 film and FR-TiO_2 film on AZO, respectively. d) XRD patterns of TiO_2 film and FR-TiO_2 film deposited on glass. e) Characterization of conductivity of TiO_2 and FR-TiO_2 films. f) UPS measurements for TiO_2 and FR-TiO_2 film on FTO. g) Energy level diagram of TiO_2, FR-TiO_2, and perovskite.

methyl ester (PCBM)/Au and then performed the space-charge limited current (SCLC) measurement(**Figure 5**a,b).[35,36] The defect densities were calculated by fitting the curves to obtain V_{TFL} and then substituting them into the Equation 1:

$$V_{TFL} = eL^2 N_{trap}/2\varepsilon_0\varepsilon_r \quad (1)$$

where the V_{TFL}, e, L, ϵ_0 and ϵ_r are the trap-filled limit voltage, elementary charge, thickness of perovskite films, permittivity of vacuum, and dielectric constant of the perovskite, respectively. We calculated the defect density of perovskite films for devices based on TiO_2 and FR-TiO_2 to be 1.24×10^{16} and 8.42×10^{15} cm^{-3}, respectively. The reduced defect density should result from the optimized perovskite crystallization and the perovskite/ETL interface. Steady-state photoluminescence (SSPL) spectroscopy and time-resolved photoluminescence (TRPL) were utilized to investigate the charge carrier dynamics of the perovskite films deposited on different ETLs. As shown in Figure 5c, the PL intensity of perovskite film on FR-TiO_2 shows an obvious sequence, indicating accelerated interfacial electron transport. In Figure 5d, by fitting the TRPL spectra of perovskite films according to a biexponential decay (Table S3, Note S2, Supporting Information), the average carrier lifetime of perovskite film on FR-TiO_2 is 263 ns, which is much shorter than that (613 ns) of the perovskite film on TiO_2, validating the accelerated interfacial electron transport.

The carrier transport dynamics and physical properties of PSCs with SnO_2 and FR-TiO_2 were characterized by measurements of electrochemical impedance spectroscopy (EIS) and ideal factor calculation. Figure 5e shows the EIS spectra obtained in ambient air under dark conditions, with fitting information shown in Table S4 (Supporting Information). It is reported that the semicircle in the high-frequency region responds to impedance (*Rct*) arising from the charge transport between the electron (hole) transport layer with the perovskite layer, and the semicircle in the low-frequency region is associated with the carrier recombination impedance (*Rre*).[37] The EIS spectra of

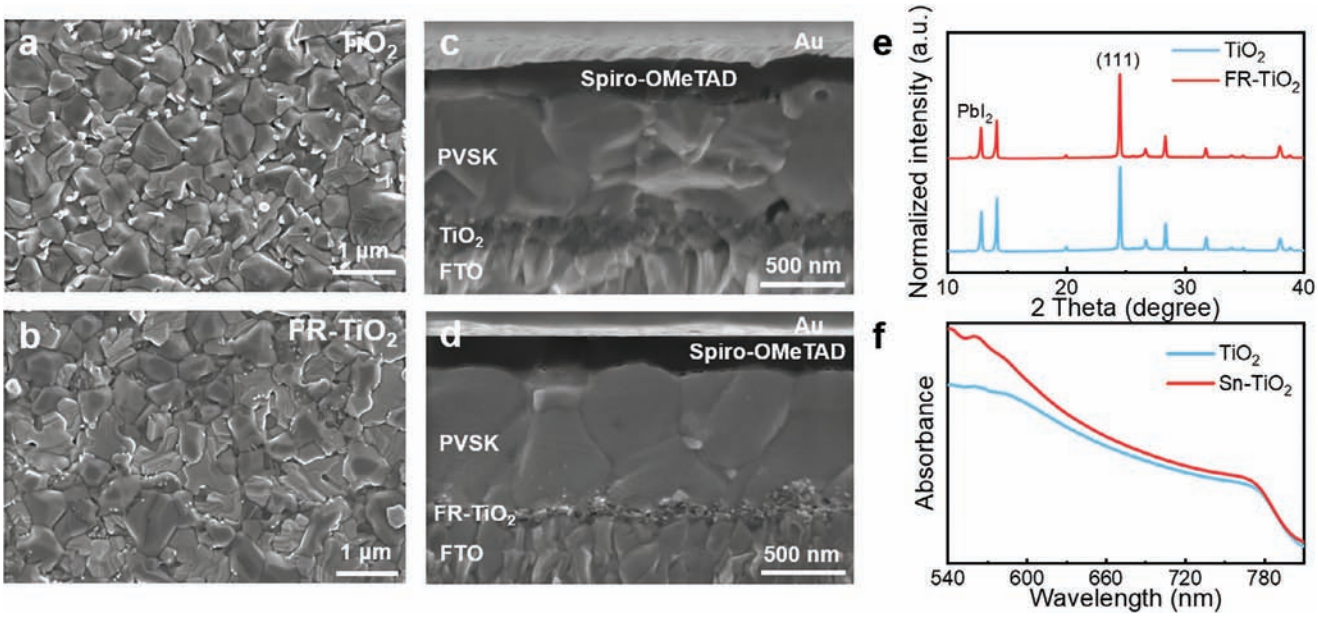

Figure 4. a,b) Top-view SEM images of perovskite films deposited on TiO_2 and FR-TiO_2 films. c,d) Cross-sectional SEM images of perovskite films deposited on TiO_2 and FR-TiO_2 films. e) XRD patterns of perovskite films deposited on TiO_2 film and FR-TiO_2 film. f) UV–vis absorption spectra of perovskite films on TiO_2 and FR-TiO_2 films.

PSCs with FR-TiO_2 exhibit a smaller *R*ct and a larger *R*re, indicating the optimized interface contact and reduced carrier recombination within the device. Besides, we calculated the ideal factor (n_{ID}) of PSCs with TiO_2 and FR-TiO_2 to evaluate their defect-induced carrier recombination according to the formula: *V*OC = nIDkB*T*(ln *P*light)/q + constant, where nID is the ideal factor, kB is the Boltzmann's constant, *T* is the temperature and q is the elementary charge.[38] As shown in Figure 5f, the PSC with FR-TiO_2 exhibits a nID of 1.2, which is smaller than that (1.35) of PSCs with TiO_2, indicating the reduced defect-induced

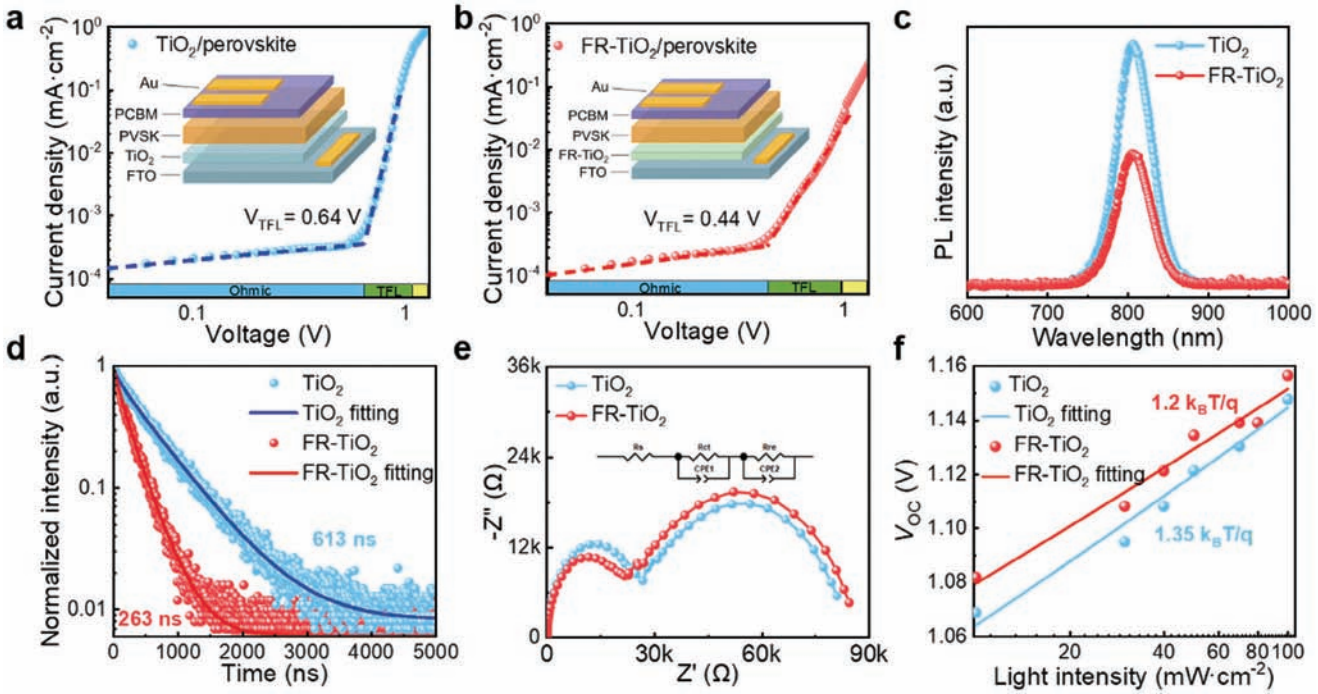

Figure 5. a,b) SCLC curves for electron-only devices. c,d) SSPL and TRPL spectra of perovskite films on TiO_2 and FR-TiO_2. e) EIS spectra of planar PSCs with various ETLs. f) The relationship between the V_{OC} of PSCs and light intensity.

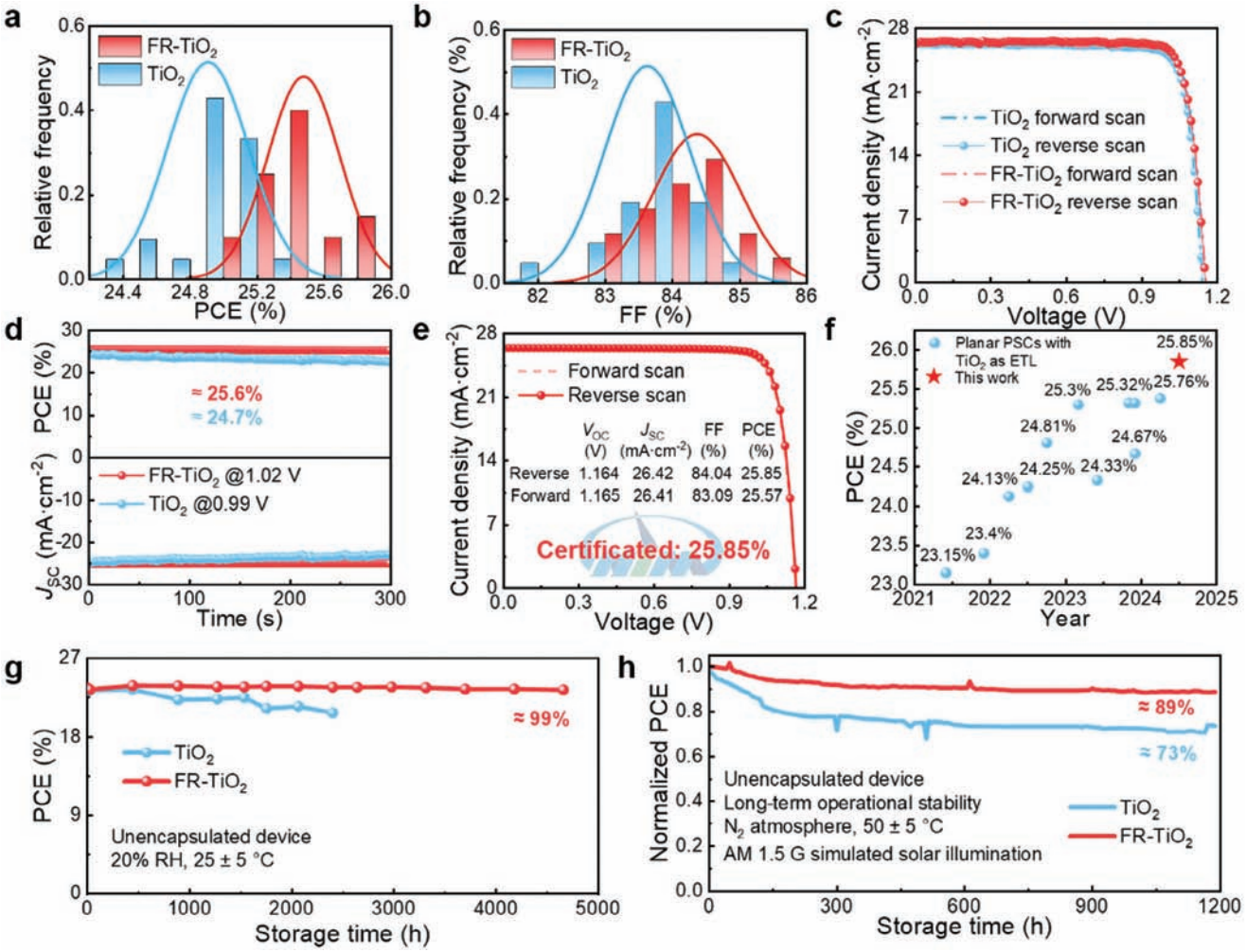

Figure 6. a) Statistical results of PCEs (reverse scan) fitted from 20 planar PSCs with various ETLs. b) Statistical results of FFs (reverse scan) fitted from 20 planar PSCs with various ETLs. c) *J–V* curves (forward and reverse scan) of champion planar PSCs with TiO_2 and FR-TiO_2, the active area of the cells is 0.1 cm^2. d) Steady-state efficiency at the maximum power point for PSCs with different ETLs. e) *J–V* curves measured at the National Institute of Metrology, an independent solar cell-accredited laboratory. f) PCE comparison between our PSC and reported PSCs, the active area of these PSCs is ≈0.1 cm^2. g) Stability tracking of cells in the air for 4656 h. h) Operational stability tracking of cells under steady-state light illumination and bias voltage for 1188 h.

carrier recombination. These results confirm that the FR-TiO_2 can optimize the interface contact, accelerate the interfacial electron transport, and reduce the defect-induced carrier recombination, potentially enhancing the efficiency of PSCs.

2.3. Improved Performance of PSCs

We fabricated planar PSCs with TiO_2 and FR-TiO_2 and characterized their photovoltaic performance, the structure is shown in Figure S9 (Supporting Information). The Statistical charts of photovoltaic parameters from 20 PSCs with TiO_2 and FR-TiO_2, respectively, are shown in **Figures** 6a,b and S10 (Supporting Information). The PCE distribution histograms indicate that the PSCs with TiO_2 and FR-TiO_2 both exhibit good reproducibility, which should result from the well-regulated TiO_2 deposition process. In Figure 6a, the average efficiency of PSCs increases from 24.91% for TiO_2 ETL to 25.48% for FR-TiO_2 ETL mainly resulting from the increased average fill factor (FF). In detail, the average J_{SC} of PSCs with FR-TiO_2 is 26.30 mA cm^{-2}, higher than that (26.03 mA cm^{-2}) of PSCs with TiO_2, which may be attributed to the blue shift in the absorption edge and the increased light transmittance of FR-TiO_2, as confirmed by external quantum efficiency characterization (Figure S11, Supporting Information), which demonstrated that FR-TiO_2 film exhibited significantly stronger light absorption in the 400–900 nm range compared to the TiO_2 film. The FF of PSCs with FR-TiO_2 is also effectively increased, the average FF is 84.32%, and the highest FF is even up to 85.7%. This increased FF should contribute to the improved conductivity of TiO_2 and optimized interface contact. The PSCs with FR-TiO_2 achieve a champion PCE of 25.81% with J_{SC} of 26.37 mA cm^{-2}, V_{OC} of 1.15 V, and FF of 85.3% (Figure 6c, Table S5, Supporting Information). In comparison, the PSCs with TiO_2 achieve a champion PCE of 25.20% with J_{SC}

of 26.34 mA cm^{-2}, V_{OC} of 1.13 V, and FF of 83.56%. The stabilized PCE of both PSCs was also measured (Figure 6d; Figure S12, Supporting Information), the stabilized PCE for FR-TiO_2-based PSC is certificated to be 25.5%, which shows a negligible decrease after tracking for 300 s. Encouragingly, one of the best-performing PSCs with FR-TiO_2 ETL was sent to a third-independent institute of the National Institute of Metrology for certification. As shown in Figure 6e and Figure S12 (Supporting Information), the PSCs with FR-TiO_2 achieve a certificated PCE of 25.85% with J_{SC} of 26.42 mA cm^{-2}, V_{OC} of 1.64 V, and FF of 84.04%. We conducted a PCE comparison among the reported works that fabricated planar PSCs using TiO_2 as the ETL (Figure 6f, Table S6, Supporting Information). Our certificated PCE of 25.85% is the highest value among the TiO_2-based planar PSCs, which significantly promotes the advance of TiO_2-based planar PSCs, indicating the positive effect of our deposition regulation on improving the photovoltaic performance of PSCs.

Finally, the air and operational stability of PSCs using different ETLs have been investigated, as shown in Figure 6g,h. For air stability, the unencapsulated devices were stored in the ambient condition with relative humidity of 20% at 25 ± 5 °C and the PCE was monitored. As shown in Figure 6g, the PSC with FR-TiO_2 maintains 99% of its initial PCE after storage for 4656 h, showing a negligible efficiency decline. In comparison, the PSC with TiO_2 shows an obvious efficiency decline after storage no more than 3000 h. For operational stability, the PSC with FR-TiO_2 retains ≈89% of its initial PCE after continuous operation under one sun illumination at the maximum power point for 1188 h, while the PSC with TiO_2 only retains ≈73% of its initial PCE (Figure 6h). In summary, the stability tests confirm that the FR-TiO_2 positively affects PSCs' stability, which should be attributed to the optimized interface contact and perovskite crystallization.

3. Conclusion

In this work, we propose a flocculating-regulated TiO_2 deposition to optimize the surface microstructure and improve the electrical property of Sn-doped TiO_2 ETL, achieving an impressive photovoltaic performance of planar PSCs. Compared with TiO_2, FR-TiO_2 is more compact and smoother with reduced surface roughness, and the conductivity is also increased by ≈2.5 times. Contributing to the optimized TiO_2/perovskite interface contact and promoted interfacial electron transport, the resulting planar PSCs obtained a certificated PCE of 25.85%, the highest value among the TiO_2-based planar PSCs to date. In addition, the PSCs also demonstrate enhanced long-term aging and operational stability. This work reports a simple and repeatable approach to fabricating high-quality ETL, providing more opportunities for achieving high-efficiency PSCs and other thin-film optoelectric devices.

4. Experimental Section

The experimental section is shown in the Supporting Information.

Supporting Information

Supporting Information is available from the Wiley Online Library or from the author.

Acknowledgements

This work was supported partially by the Key Research and Development Program sponsored by the Ministry of Science and Technology (MOST) (Grant nos. 2022YFB4200301), the National Natural Science Foundation of China (Grant nos. 52232008, 51972110, 52102245, 52072121, 52402254 and 22409061), the Beijing Natural Science Foundation (2222076, 2222077), the Beijing Nova Program (20220484016), Young Elite Scientists Sponsorship Program by CAST (2022QNRC001), 2022 Strategic Research Key Project of Science and Technology Commission of the Ministry of Education, the Huaneng Group Headquarters Science and Technology Project (HNKJ20-H88), the State Key Laboratory of Alternate Electrical Power System with Renewable Energy Sources (LAPS2024-05), the Fundamental Research Funds for the Central Universities (2022MS029, 2022MS02, 2022MS031, 2023MS042, 2023MS047) and the NCEPU "Double First-Class" Program.

Conflict of Interest

The authors declare no conflict of interest.

Author Contributions

H.Y. and X.Z. contributed equally. H.Y. and H.H. conceived the idea. M.L. and X.Z. guided the work as a supervisor. H.Y. and H.H. did experimental designs, device fabrication, and data analysis. D.W., P.Z., and D.L. participated in the device fabrications and some material and device characterizations. B.F., Y.Y., and Y.Q. supported the measurement system construction, device fabrication, characterization, and discussions. B.F., H.H., and M.L. participated in manuscript writing and revising. Q.G., P.C., Y.Y., and Z.L. polished the manuscript language. All authors were involved in the discussions and approved the manuscript.

Data Availability Statement

The data that support the findings of this study are available from the corresponding author upon reasonable request.

Keywords

deposition regulation, doping, electron transport layer, perovskite solar cells, TiO_2

Received: July 22, 2024
Revised: September 25, 2024
Published online:

[1] H. Chen, C. Liu, J. Xu, A. Maxwell, W. Zhou, Y. Yang, Q. Zhou, A. S. R. Bati, H. Wan, Z. Wang, L. Zeng, J. Wang, P. Serles, Y. Liu, S. Teale, Y. Liu, M. I. Saidaminov, M. Li, N. Rolston, S. Hoogland, T. Filleter, M. G. Kanatzidis, B. Chen, Z. Ning, E. H. Sargent, *Science* **2024**, *384*, 189.
[2] H. Huang, H. Yan, M. Duan, J. Ji, X. Liu, H. Jiang, B. Liu, S. Sajid, P. Cui, Y. Li, M. Li, *Appl. Surf. Sci.* **2021**, *544*, 148583.
[3] Q. Jiang, L. Zhang, H. Wang, X. Yang, J. Meng, H. Liu, Z. Yin, J. Wu, X. Zhang, J. You, *Nat. Energy* **2016**, *2*, 16177.
[4] Z. Wang, X. Zhu, J. Feng, C. Wang, C. Zhang, X. Ren, S. Priya, S. (Frank) Liu, D. Yang, *Adv. Sci.* **2021**, *8*, 2002860.
[5] J. Zhou, L. Tan, Y. Liu, H. Li, X. Liu, M. Li, S. Wang, Y. Zhang, C. Jiang, R. Hua, W. Tress, S. Meloni, C. Yi, *Joule* **2024**, *8*, 1691.

[6] Z. Lan, H. Huang, S. Du, Y. Lu, C. Sun, Y. Yang, Q. Zhang, Y. Suo, S. Qu, M. Wang, X. Wang, L. Yan, P. Cui, Z. Zhao, M. Li, *Angew Chem. Int. Ed.* **2024**, *136*, 202402840.
[7] D. Wei, J. Ji, D. Song, M. Li, P. Cui, Y. Li, J. M. Mbengue, W. Zhou, Z. Ning, N.-G. Park, *J. Mater. Chem. A* **2017**, *5*, 1406.
[8] J. Ji, X. Liu, H. Jiang, M. Duan, B. Liu, H. Huang, D. Wei, Y. Li, M. Li, *iScience* **2020**, *23*, 101013.
[9] A. Yella, L.-P. Heiniger, P. Gao, M. K. Nazeeruddin, M. Grätzel, *Nano Lett.* **2014**, *14*, 2591.
[10] J. Burschka, N. Pellet, S.-J. Moon, R. Humphry-Baker, P. Gao, M. K. Nazeeruddin, M. Grätzel, *Nature* **2013**, *499*, 316.
[11] G. E. Eperon, V. M. Burlakov, A. Goriely, H. J. Snaith, *ACS Nano* **2014**, *8*, 591.
[12] Z. Sun, J. H. Kim, Y. Zhao, F. Bijarbooneh, V. Malgras, Y. Lee, Y.-M. Kang, S. X. Dou, *J. Am. Chem. Soc.* **2011**, *133*, 19314.
[13] H. Huang, P. Cui, Y. Chen, L. Yan, X. Yue, S. Qu, X. Wang, S. Du, B. Liu, Q. Zhang, Z. Lan, Y. Yang, J. Ji, X. Zhao, Y. Li, X. Wang, X. Ding, M. Li, *Joule* **2022**, *6*, 2186.
[14] Z. Wu, Y. Wang, L. Li, R. Zhang, J. Hong, R. Huang, L. Che, G. Yang, H. Rao, Z. Pan, X. Zhong, *Small* **2023**, *19*, 2300690.
[15] J. Luo, J. Chen, B. Wu, T. W. Goh, W. Qiao, Z. Ku, H. B. Yang, L. Zhang, T. C. Sum, B. Liu, *Chem* **2018**, *4*, 911.
[16] M. Abuhelaiqa, N. Shibayama, X.-X. Gao, H. Kanda, M. K. Nazeeruddin, *ACS Appl. Energy Mater.* **2021**, *4*, 3424.
[17] Y. You, W. Tian, L. Min, F. Cao, K. Deng, L. Li, *Adv. Mater. Interfaces* **2020**, *7*, 1901406.
[18] N. Kumari, J. V. Gohel, S. R. Patel, *Mater. Sci. Semicond. Process.* **2018**, *75*, 149.
[19] K.-T. Chen, C.-H. Hsu, S.-C. Jiang, L.-S. Liang, P. Gao, Y. Qiu, W.-Y. Wu, S. Zhang, W.-Z. Zhu, S.-Y. Lien, *IEEE Trans. Electron Devices* **2022**, *69*, 1149.
[20] Y. Hu, L. Li, Z. Zhang, S. Gao, J. Guo, P. Yang, *Chem. Phys. Lett.* **2022**, *803*, 139830.
[21] S. Sharma, N. Soleimanioun, R. Kaur, M. Rani, S. K. Tripathi, *Mater. Chem. Phys.* **2021**, *257*, 123730.
[22] Y. Tang, R. Roy, Z. Zhang, Y. Hu, F. Yang, C. Qin, L. Jiang, H. Liu, *Sol. Energy* **2022**, *231*, 440.
[23] D. Wang, T. He, S. Li, Y. Jiang, M. Yuan, *ACS Appl. Energy Mater.* **2022**, *5*, 5340.
[24] Y. Duan, G. Zhao, X. Liu, J. Ma, S. Chen, Y. Song, X. Pi, X. Yu, D. Yang, Y. Zhang, F. Guo, *Nanotechnology* **2021**, *32*, 245201.
[25] W. Hu, Z. Wen, X. Yu, P. Qian, W. Lian, X. Li, Y. Shang, X. Wu, T. Chen, Y. Lu, M. Wang, S. Yang, *Adv. Sci.* **2021**, *8*, 2004662.
[26] H. Tan, A. Jain, O. Voznyy, X. Lan, F. P. García De Arquer, J. Z. Fan, R. Quintero-Bermudez, M. Yuan, B. Zhang, Y. Zhao, F. Fan, P. Li, L. N. Quan, Y. Zhao, Z.-H. Lu, Z. Yang, S. Hoogland, E. H. Sargent, *Science* **2017**, *355*, 722.
[27] J. Peng, F. Kremer, D. Walter, Y. Wu, Y. Ji, J. Xiang, W. Liu, T. Duong, H. Shen, T. Lu, F. Brink, D. Zhong, L. Li, O. Lee Cheong Lem, Y. Liu, K. J. Weber, T. P. White, K. R. Catchpole, *Nature* **2022**, *601*, 573.
[28] H. Min, D. Y. Lee, J. Kim, G. Kim, K. S. Lee, J. Kim, M. J. Paik, Y. K. Kim, K. S. Kim, M. G. Kim, T. J. Shin, S. Il Seok, *Nature* **2021**, *598*, 444.
[29] J. J. Yoo, G. Seo, M. R. Chua, T. G. Park, Y. Lu, F. Rotermund, Y.-K. Kim, C. S. Moon, N. J. Jeon, J.-P. Correa-Baena, V. Bulović, S. S. Shin, M. G. Bawendi, J. Seo, *Nature* **2021**, *590*, 587.
[30] P. V. Kamat, *Chem. Rev.* **1993**, *93*, 267.
[31] Y. Zhao, F. Ma, Z. Qu, S. Yu, T. Shen, H.-X. Deng, X. Chu, X. Peng, Y. Yuan, X. Zhang, J. You, *Science* **2022**, *377*, 531.
[32] X. Yang, D. Luo, Y. Xiang, L. Zhao, M. Anaya, Y. Shen, J. Wu, W. Yang, Y. Chiang, Y. Tu, R. Su, Q. Hu, H. Yu, G. Shao, W. Huang, T. P. Russell, Q. Gong, S. D. Stranks, W. Zhang, R. Zhu, *Adv. Mater.* **2021**, *33*, 2006435.
[33] E. L. Lim, Z. Wei, *J. Energy Chem.* **2024**, *90*, 504.
[34] J. Liang, X. Hu, C. Wang, C. Liang, C. Chen, M. Xiao, J. Li, C. Tao, G. Xing, R. Yu, W. Ke, G. Fang, *Joule* **2022**, *6*, 816.
[35] F.-C. Chiu, *Adv. Mater. Sci. Eng.* **2014**, *2014*, 578168.
[36] A. Many, G. Rakavy, *Phys. Rev.* **1962**, *126*, 1980.
[37] J. Chen, X. Zhao, S. Kim, N. Park, *Adv. Mater.* **2019**, *31*, 1902902.
[38] C. M. Proctor, M. Kuik, T.-Q. Nguyen, *Prog. Polym. Sci.* **2013**, *38*, 1941.